Journal of Marine Science and Technology

Volume 23 | Issue 5 Article 7

FLOW CHARACTERISTICS OF SPILLING AND PLUNGING BREAKERS IN THE SURF ZONE

Ting-Chieh Lin
Department of Hydraulic and Ocean Engineering, National Cheng Kung University, Tainan, Taiwan, R.O.C. Tainan Hydraulics Laboratory/International Wave Dynamics Research Center, National Cheng Kung University, Tainan County, Taiwan, R.O.C.

Han-Lun Wu
Department of Hydraulic and Ocean Engineering, National Cheng Kung University, Tainan, Taiwan, R.O.C.

Shih-Ming Lo
Department of Hydraulic and Ocean Engineering, National Cheng Kung University, Tainan, Taiwan, R.O.C.

Shih-Chun Hsiao
Department of Hydraulic and Ocean Engineering, National Cheng Kung University, Tainan, Taiwan, R.O.C., schsiao@mail.ncku.edu.tw

Hwung-Hweng Hwung
Department of Hydraulic and Ocean Engineering, National Cheng Kung University, Tainan, Taiwan, R.O.C.

Recommended Citation

Lin, Ting-Chieh; Wu, Han-Lun; Lo, Shih-Ming; Hsiao, Shih-Chun; and Hwung, Hwung-Hweng (2015) "FLOW CHARACTERISTICS OF SPILLING AND PLUNGING BREAKERS IN THE SURF ZONE," *Journal of Marine Science and Technology*: Vol. 23: Iss. 5, Article 7.
DOI: 10.6119/JMST-015-0409-2
Available at: https://jmstt.ntou.edu.tw/journal/vol23/iss5/7

FLOW CHARACTERISTICS OF SPILLING AND PLUNGING BREAKERS IN THE SURF ZONE

Acknowledgements

This research was supported by National Science Council of Taiwan under grants NSC 101-2628-E-006-015-MY3, MOST 104-2911-I-006-301 (International Wave Dynamics Research Center), MOST 103-2221-E-006-229-MY3 and the Open Fund from the State Key Laboratory of Hydraulics and Mountain River Engineering, Sichuan University (SKHL1308).

Journal of Marine Science and Technology, Vol. 23, No. 5, pp. 638-648 (2015)
DOI: 10.6119/JMST-015-0409-2

FLOW CHARACTERISTICS OF SPILLING AND PLUNGING BREAKERS IN THE SURF ZONE

Ting-Chieh Lin[1, 2], Han-Lun Wu[1], Shih-Ming Lo[1], Shih-Chun Hsiao[1], and Hwung-Hweng Hwung[1]

Key words: RANS model, spilling breaker, plunging breaker, surf zone, streamline, vorticity.

ABSTRACT

Fundamental flow characteristics in the surf zone of spilling (SP) and plunging (PL) breakers are compared using a well-validated numerical model named COBRAS. The main objective is to investigate how beach slope affects flow characteristics (streamline topography, vorticity evolution processes, TKE dynamics and reverse flow) in the surf zone of plunging (PL) and spilling (SP) breakers. The major results are of four categories: (1) the streamline topography of PL waves is mostly similar to that of SP. For both types of breaker, a convergent stagnation point (CSP) always appears in the offshore direction after the generation of a divergent stagnation point (DSP). The location of a DSP is generally underneath the front face of wave crest. Both DSP and CSP move to the inner surf zone following wave propagation. (2) the main difference of vortices evolution is that clockwise (CW) vortices after wave breaking are stronger for PL waves but mild for SP waves . The CW vortices of SP decay upstream directly but those of PL waves advect toward the bottom slope and then degenerate upstream. (3) The TKE generated by PL waves is much larger than that generated by SP waves. The distributions of generated TKE values of SP and PL waves are similar to the corresponding vortex motions. (4) The maximum magnitude of reverse flow in surf-zone of PL waves is around 1.4 times that of SP waves.

I. INTRODUCTION

Understanding the hydrodynamics of breaking waves in surf zone is of fundamental importance since the flow motions induced by wave breaking enhance turbulence and vorticity generation, which are highly related to nearshore sediment transport and beach morphology (e.g. Battjes, 1988; Christensen et al., 2002; Longo et al., 2002; Shin and Cox, 2006; Sou and Yeh, 2011). Battjes (1974) suggested a surf similarity parameter (SSP) for defining a breaking type:

$$\xi = \frac{\tan\beta}{\sqrt{H_0 / L_0}} = \begin{cases} < 0.5 & \text{(SP)} \\ 0.5 \sim 3.3 & \text{(PL)} \\ > 3.3 & \text{(SU)} \end{cases} \quad (1)$$

where SP, PL and SU denotes spilling, plunging and surging breaking waves, respectively; $\tan\beta$ is the beach slope, and H_0 and L_0 are the offshore wave height and wavelength in deep water, respectively. In general, PL and SP are believed to be the two dominant breakers in most surf zones (Battjes, 1988; Dean and Dalrymple, 1991; Bradford, 2000; Feng and Stansby, 2005). A visible difference between PL and SP is the incipient stage when the wave breaks: SP commences within a small region nearby wave crest where white foam with nearly symmetric cap is observed; whereas PL has a wave crest whose front curls into a free jet that plunges into the sea surface and subsequently forms splash-up. Both PL and SP ultimately degenerate into relatively small-scale turbulent bores that propagate onshore.

The flow characteristics of PL and SP have been extensively investigated both experimentally and numerically in literature. Popular flow visualization approaches in a laboratory are Particle Imagine Velocimetry (PIV) (e.g. Chang and Liu, 1998, 1999; Kimmoun and Branger, 2007; Huang et al., 2009a, 2009b; Sou et al., 2010), Laser Doppler Velocimetry (LDV) (e.g. Nadaoka et al., 1989; Feng and Stansby, 2005), and Fiber-optic Laser Doppler Velocimetry (FLDV) (e.g. Ting and Kirby, 1994, 1995, 1996). However, laboratory approaches have certain limitations. For instance, traditional PIV and LDV cannot resolve flow behaviors within a highly aerated region near a wave crest mainly due to the presence of foam and bubbles generated by breaking waves (e.g. Chang and Liu, 1998; Huang et al., 2009a, 2009b). Furthermore, PIV and LDV implementations have scaling and observational diffi-

Paper submitted 08/18/14; revised 03/31/15; accepted 04/09/15. Author for correspondence: Shih-Chun Hsiao (e-mail: schsiao@mail.ncku.edu.tw).
[1] Department of Hydraulic and Ocean Engineering, National Cheng Kung University, Tainan, Taiwan, R.O.C.
[2] Tainan Hydraulics Laboratory/International Wave Dynamics Research Center, National Cheng Kung University, Tainan County, Taiwan, R.O.C.

culties. Many experimental trials must be conducted to obtain spatially integrated flow fields. Certain flow regions where the velocity gradients are extremely chaotic and vary severely in time, such as the swash zone, may not be easily observed (e.g. Sou and Yeh, 2011). Traditional LDV can be used to measure the spatial flow structures under breaking wave conditions under the assumption that the target velocity fields vary slowly (e.g. Feng and Stansby, 2005). Such an assumption is not always valid because the flow motions after wave breaking may either be severe or time-dependent. In addition, traditional LDV and FLDV cannot be used to directly compute instantaneous spatial gradients; the corresponding turbulence production and dissipation terms are therefore unavailable. Alternatively, Navier-Stokes equation-type numerical models together with a sophisticated turbulence closure solver are powerful to this topic. The flow motions after wave breaking are allowed to be fully computed and observed (e.g. Bradford, 2000; Liu and Losada, 2002; Christensen, 2006; Lubin et al., 2006).

In this paper, a well-validated Reynolds-Averaged Navier-Stokes (RANS) model, called "Cornell Breaking And Structure (COBRAS)," is applied to investigate the fundamental flow characteristics in the surf zone of PL and SP (for model details see Chap. 2). The main objective is to investigate how beach slope affects the flow characteristics of PL and SP. Numerical experiments are carefully performed to study (1) the streamline topography in a breaking wave circle, (2) vorticity generation/evolution processes and the vorticity structures after wave breaking, (3) TKE generation/dissipation and (4) vertical profile of horizontal velocity of reverse flow during run-down phases. It should be noted that detailed descriptions of streamline topography and vorticity structure under wave breaking conditions are still limited in literature. We also explain the difference between laboratory work of Feng and Stansby (2005) and our numerical results. Chapter 2 validates the COBRAS model by reproducing the spilling breaker experiment of Huang et al. (2009b). Laboratory data of an identical experiment reported by Huang et al. (2009b) and Huang (2010) are also compared. Chapter 3 describes a set of numerical investigations of flow characteristics in a surf zone subjected to SP and PL waves. Hydrodynamic discrepancies are discussed in detail. Chapter 4 concludes this paper.

II. DESCRIPTION AND VALIDATION OF COBRAS MODEL

1. Numerical Model Background

The COBRAS model solves two-dimensional RANS equations using a finite difference two-step projection method. The nonlinear turbulence $k-\varepsilon$ closure model is employed to compute the TKE and the free surface deformation is tracked using the VOF method. The technique of partial cell treatment with an openness coefficient is used to treat obstacle as a special case of the flow with an infinite density. The zero-stress and zero-pressure conditions are applied to the mean free surface for neglecting the air-flow interaction. The computational mesh can be a multi-grid system, allowing a region of interest/unimportance to be discretized using finer/courser meshes. The model details were given in numerous studies (e.g. Lin and Liu, 1998a, 1998b; Losada et al., 2008; Hsiao and Lin, 2010; Wu et al., 2012; Wu and Hsiao, 2013; Wu et al., 2014) and thus not repeated here.

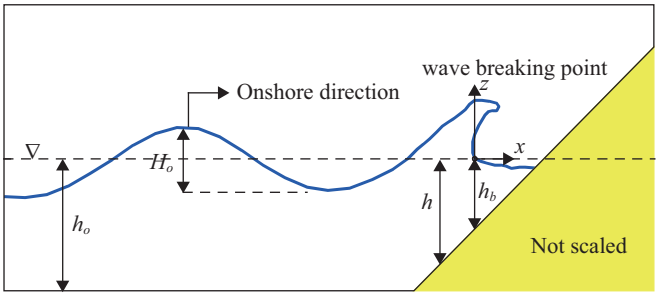

Fig. 1. Sketch of definitions used in the present study.

2. Experimental and Numerical Conditions

Huang et al. (2009a), Huang et al. (2009b) and Huang (2010) performed an identical experiment to systematically and quantitatively investigate the free surface evolutions and velocity fields (Huang et al., 2009b), turbulence generation and evolution (Huang et al., 2009a, 2009b) and streamline topography (Huang, 2010) in a laboratory surf zone under SP conditions using PIV. The complete laboratory description can be found in Huang (2010). According to Huang et al. (2009a), a monochromatic water-wave train was generated to propagate offshore. The wave became SP on a 1:20 ($\tan\beta$ = 1/20) uniform slope. The offshore water depth h_0 was 0.359 m, the offshore wave height H_0 was 0.03 m, the wave period T was 1.0 s, the offshore wave length L was 1.56 m (computed using the dispersion relationship of linear wave theory), the breaking wave height H_b was 0.0364 m, and the breaking water depth h_b was 0.048 m. The flow quantities in the surf-zone were obtained by overlapping 7 individual fields of view (FOVs). The experimental conditions indicate that SSP = 0.36, which agrees with the value predicted by Eq. (1).

Fig. 1 shows the setup of the present computational domain, where x and z are defined as the abscissa and ordinate starting from the point where the wave breaks, respectively. A 2D wave flume with length x = 24.0 m and depth z = 0.4 m was numerically created to reproduce the experiment of Huang et al. (2009b). An impermeable beach with a uniform slope of 1:20 was built starting at x = 16.7 m. The computational mesh was discretized with two non-uniform meshes in the x- direction applied in front of (Δx = 0.01 m) and behind (Δx = 0.005 m) the toe of the sloping beach, and one uniform mesh in the z- direction (Δz = 0.0025 m) applied throughout the vertical domain. A total of 3132 × 162 computational cells were generated. Preliminary tests were performed to ensure that the numerical results are grid independent. The Courant number was defined as 0.3 for all simulations. Stokes second-order

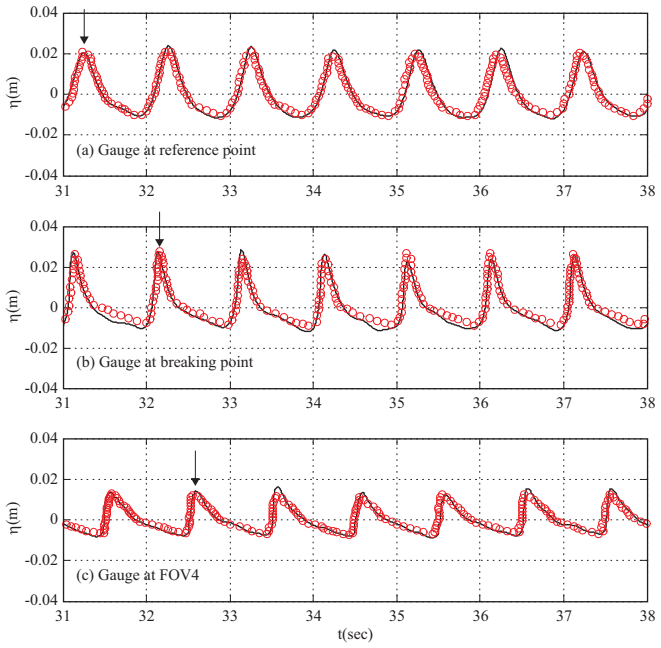

Fig. 2. Comparison of wave gauges between numerical results (solid line) and laboratory data (○) of Huang et al. (2009b).

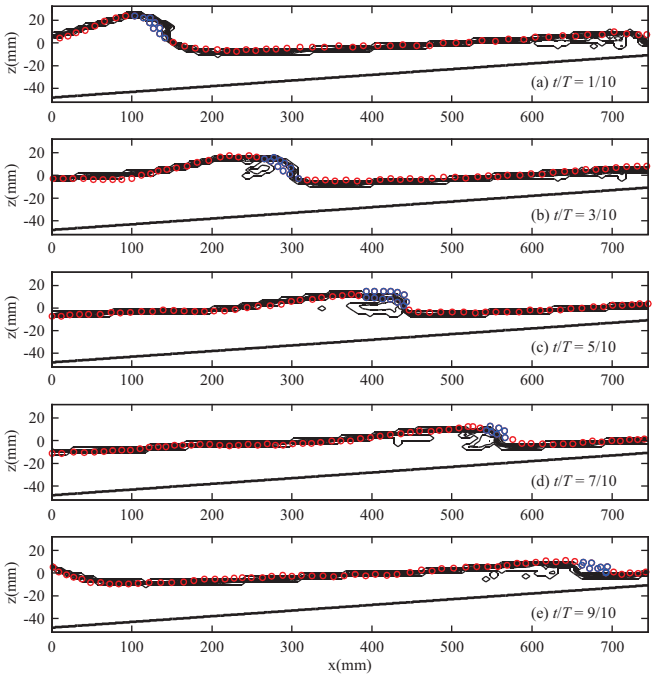

Fig. 3. Spatial snapshot comparison between numerical results (solid line) and laboratory data (○) of Huang et al. (2009a). Note that the laboratory regions of air bubbles are marked by blue circles. 10 contours of the VOF function with an interval of 0.1 from 0.1 to 1.0 are plotted using black solid lines.

wave trains were chosen based on the incident wave conditions (Dean and Dalrymple, 1991), sent from the left boundary into the computational domain. A simulation was executed for 40 wave periods to reach a quasi steady-state of wave deformation. For the $k-\varepsilon$ model, the coefficients suggested by Lin and Liu (1998a; 1998b) were adopted. The interaction between air and fluid was neglected. No-slip boundary conditions and partial cell treatment were applied at the solid surfaces.

3. Comparison of Free Surface and Spatial Snapshots

Fig. 2 shows surface elevations obtained at three important locations (i.e. the reference point, the breaking point and the post breaking in FOV4) using the numerical results and the data of Huang et al. (2009b). Good agreements for wave phases and wave deformations (tracked wave is denoted by arrows in Fig. 2) were observed, suggesting that the numerical results are reliable. Fig. 3 presents overall agreements of typical stages of spatial wave evolutions (i.e. wave shoaling, wave breaking, bore formation and bore run-up) between numerical results and Huang et al. (2009b). It can be seen that COBRAS model exhibits a good capability for capturing the location and phase of wave breaking (Figs. 3(a) and (b)) as well as the subsequent run-up motion of a turbulent bore (Figs. 3(c)-(e)). Noticeably, numerical results using 10 contour lines of the volume-fraction of water from 0.1 to 1.0 are also drawn to "qualitatively" represent the entrapped air-bubbles during wave breaking, showing the existence of "fictitious air entrapments" in model computations. We have to note that even though the real entrapped air effects are not considered in the COBRAS model, such a representation skill was successfully employed by Zhang and Liu (2008) and Hsiao and Lin (2010) to qualitatively examine entrapped air phenomena under turbulent bores. The numerical contours with various values of θ show that a transient and typical spilling phase with a "white cap" (also shown by blue circles for laboratory data) being generated and stretched upstream (Figs. 3(b)-(d)). These numerical contours thereby supplement the laboratory data. The blue circles shown in Fig. 3 represent the spatial envelopes of free surface within aerated regions in the laboratory; however, the corresponding velocity fields are absent because of the presence of air-bubbles (will be shown in Fig. 4). The wave phase speed during the wave run-up stage is slightly slower than that in the experimental data (Figs. 3(d) and 3(e)). Similar results were also found in Jiang et al. (2011). The overall agreements suggest that the COBRAS model is reliable.

4. Comparison of Velocity Fields

Fig. 4 compares the corresponding velocity fields of Fig. 3 obtained from the laboratory data of Huang et al. (2009b) and those obtained using the COBRAS model. At $t/T = 1/10$, the computed wave crest moves faster than that from the laboratory data. The computed results give a maximum velocity near the wave crest of 0.95 m/s. The numerically obtained velocities of 0.2~0.25 m/s (denoted by the yellow region) are broader than those measured in experiments. Interestingly, a region exists right below the wave crest ($x = 160$ mm) where the velocities are low. The magnitudes of velocities are nearly of the same order, but their directions are opposite, which is

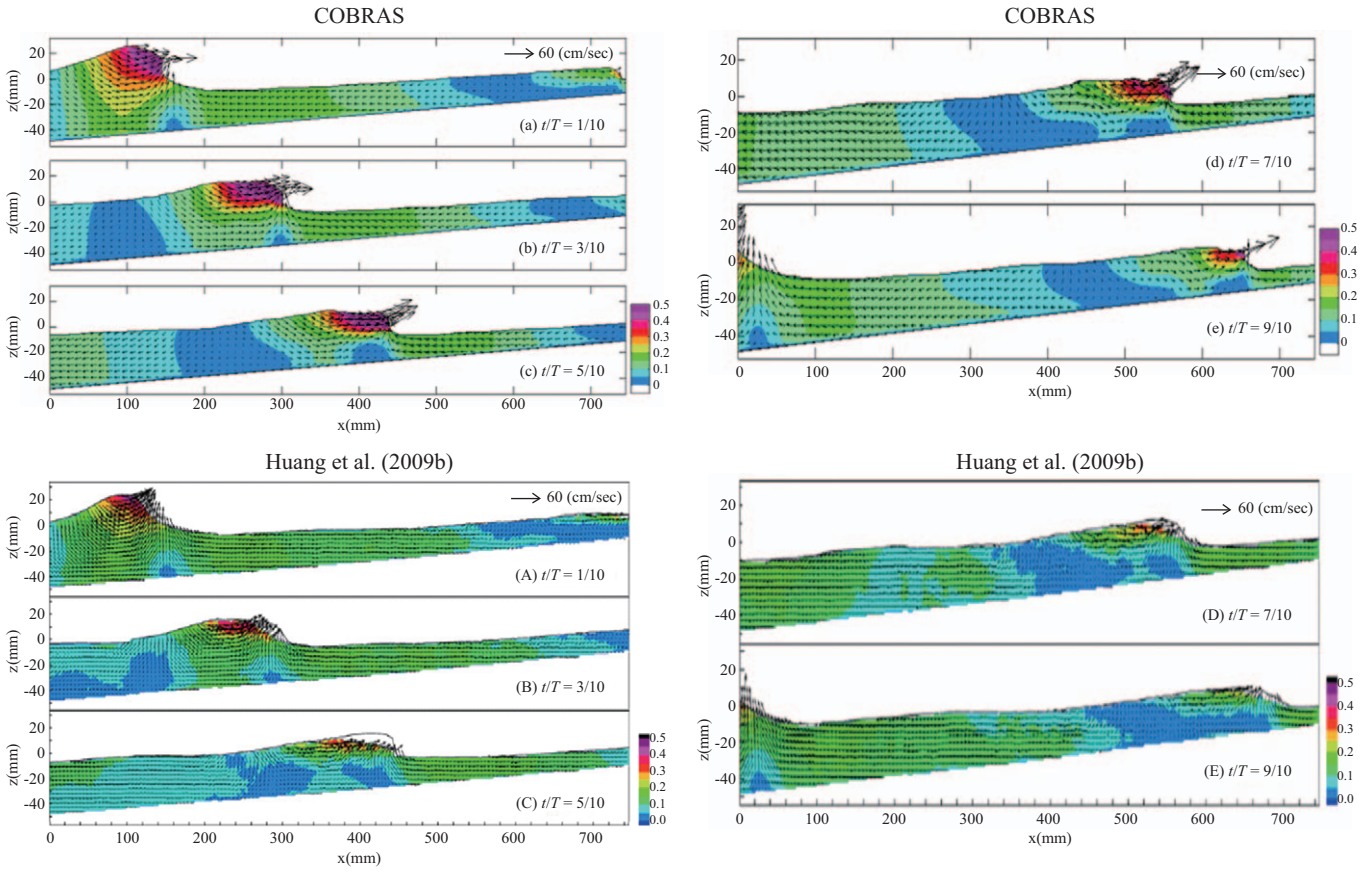

Fig. 4. Scaled ensemble-averaged horizontal velocities under crest phases. Comparison of velocity distribution obtained using the COBRAS model and that from the data of Huang et al. (2009b).

due to the interaction between onshore waves and reverse flows of previous breaking waves. Note that such flow motions contribute to the formation of a stagnation point, at which the fluid velocity approaches zero (see Chapter 3). After the waves approach inland, the low-speed region shown at t/T = 1/10 gradually becomes larger and moves upstream (Figs. 4(b) and (c)). The computed velocities within the wave crest are on the order of $O(0.5)$ m/s, for which the laboratory data are lacking (Figs. 4(b) and (c)). During t/T = 7/10 to t/T = 9/10, the numerical results indicate that the high-speed region of the wave crest becomes concentrated in a small region near the wave crest where the velocity magnitude is $O(0.6)$ m/s. The low-speed regions below and behind the wave crest gradually merge, showing behavior similar to that exhibited by the laboratory data. Overall, the COBRAS model has good agreement with the laboratory data, and provides certain velocity fields for which experimental measurements are infeasible.

5. Comparison of Velocity Profiles in the Surf Zone

Fig. 5 compares a sequence of vertical velocity distributions under crest phase in the surf zone obtained from the laboratory data of Huang (2010) and the numerical results, which were normalized by $\sqrt{gh}$. Overall agreements were found. At t/T = 0/10 and t/T = 2/10, the horizontal velocities

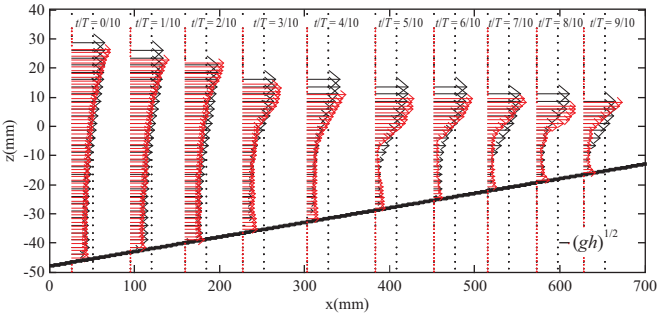

Fig. 5. Comparison of horizontal velocity distribution obtained from numerical results (black arrows) and laboratory data of Huang (2010) (red arrows). The numerical results were normalized by $\sqrt{gh}$.

are quite uniform; the velocities increase with decreasing water depth. However, in the inner surf zone, there is a considerable increase in the velocity gradients, explaining why the low-speed regions move upstream following wave propagation (see Figs. 4(c)-(e)). Such a phenomenon also implies a high possibility of vorticity generation due to strong velocity gradients (discussed in Chap. 3). At t/T = 3/10~9/10 strong velocities are observed near the wave crest.

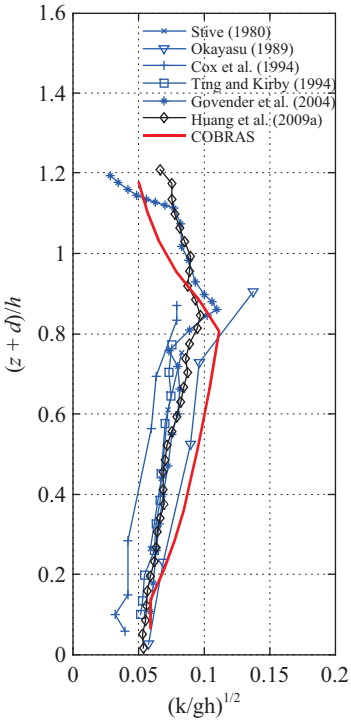

Fig. 6. Comparison of Froude-scale-normalized TKE at x = 270 mm and h/h_b~0.7.

Despite the agreements given in Fig. 5, the laboratory velocities near the bottom are stronger than those predicted by the numerical results. It can be explained using Stokes boundary layer theory that the boundary layer thickness δ_s for the present case is estimated by $\delta_s = \sqrt{\nu T/\pi} \simeq 0.56$ (mm), where ν is the kinematic viscosity of fresh water. The velocities within the boundary layer cannot be directly computed since the minimum mesh grid size in the vertical direction is Δz = 2.5 mm. Even though the no-slip boundary conditions are applied at solid boundaries and a logarithmic-law profile is assumed, the effects of the boundary layer cannot be fully resolved in the computation. Nonetheless, the overall agreements suggest that COBRAS is capable of capturing most of the velocity gradients in the surf zone.

6. Comparison of TKE

Fig. 6 compares the ensemble-time-averaged TKE at x = 270 mm and $h/h_b \simeq 0.7$, where the computed TKE values are normalized by the Froude scale. Laboratory data from literature are included for comparison. This figure indicates that the results obtained using the COBRAS model are on the same order of magnitude as those given in the literature. Quantitatively, the numerical TKE values exhibit a trend similar to those of previously reported data. The computed TKE value is around 0.059 under the wave trough, increases to 0.11 (between the mean trough and the surface elevation levels), and then decreases to 0.05 near the wave crest. The numerical results for $(z + d)/h$ values below 0.2 show excellent agreements (maximum error of 15%) with data reported by Stive (1980), Ting and Kirby (1994), and Huang et al. (2009a). For $(z + d)/h$ = 0.2~0.7, the numerical results are closest to the results reported by Okayasu (1989). The maximum differences at $(z + d)/h$ = 0.9 and 1.2 between Huang et al. (2009a) and Okayasu (1989), and Huang et al. (2009a) and Govender et al. (2004) are 57% and 57%, respectively. Therefore, the COBRAS model is satisfactory for estimating TKE under SP conditions since the largest error for entire vertical positions is around 25% at $(z + d)/h$ 1.0 compared to the data of Huang et al. (2009b).

III. FLOW CHARACTERISTICS OF SP AND PL IN THE SURF ZONE

The previous chapter demonstrated that the COBRAS model is capable of simulating flow characteristics in the surf zone under SP-wave conditions. In this chapter, the COBRAS model is applied to simulate PL with the same wave conditions but a steeper beach slope ($\tan\beta$ = 1/10) is considered. All numerical parameters given in Chapter 2 remain the same. The corresponding SSP of PL is computed by 0.721, which agrees with the prediction obtained using Eq. (1). The main goal of this chapter is to study how the beach slope affects the flow characteristics in the surf zone under SP and PL conditions. The difference in streamline topography between the two types of breaker is first investigated. The generated vorticity patterns and the corresponding evolutions are discussed. The differences in vorticity structure after wave breaking are determined. The computed TKE and vertical profiles of horizontal velocities in the surf zones are also investigated.

1. Streamline Topography

The numbers and locations of "convergent stagnation point (CSP)" and "divergent stagnation point (DSP)" are a main concern when studying streamline topography. According to Feng and Stansby (2005), "...divergent (DSP) is used to describe flow away or divergent from the stagnation point, while convergent (CSP) describes flow towards or convergent on the stagnation point." These definitions are used in the present study. Physically, the presence of DSPs/CSPs suggests that the fluid stream flows away/toward the stagnation point, resulting in passive particles being dispersed/congregated. Sou and Yeh (2011) pointed out that DSPs/CSPs are relevant to flow separation/attachment because of the difference of pressure gradients (discussed in Section 3.2).

Fig. 7 shows computed streamline topographies of SP (Fig. 7(a)), and PL (Fig. 7(b)), and the laboratory data of Huang (2010) (Fig. 7(c)). The blue and red arrows indicate the locations of DSPs and CSPs (only those along the sloping bottom are shown), respectively. The corresponding velocity fields are also presented via a color contour. It can be clearly seen that the numerical results agree well with those of Huang (2010) for the locations of DSPs/CSPs and the streamline topography under a SP condition. At t/T = 0/10, SP com-

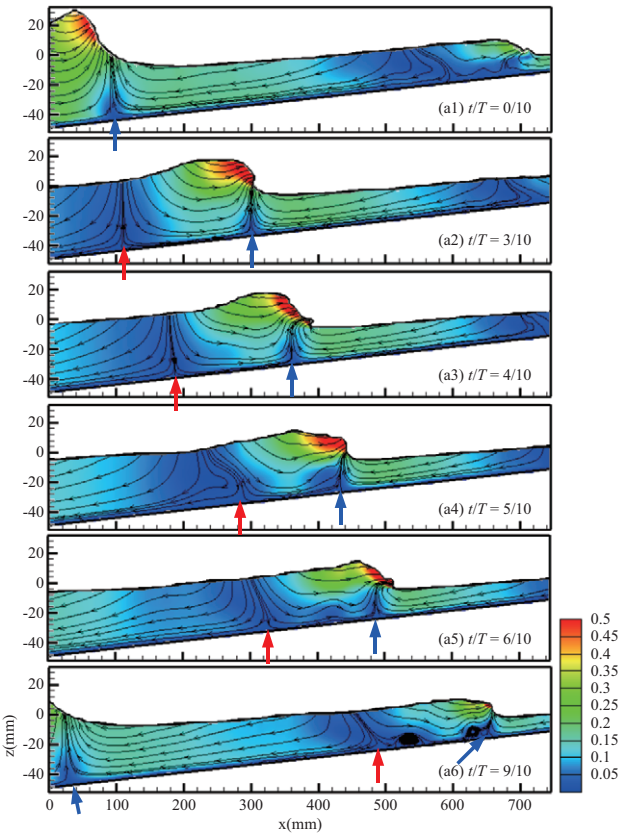

(a) SP

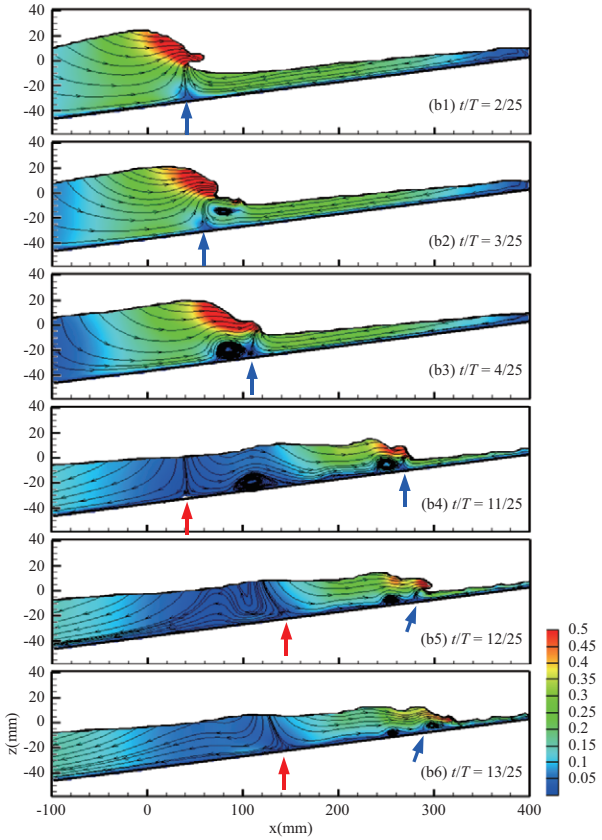

(b) PL

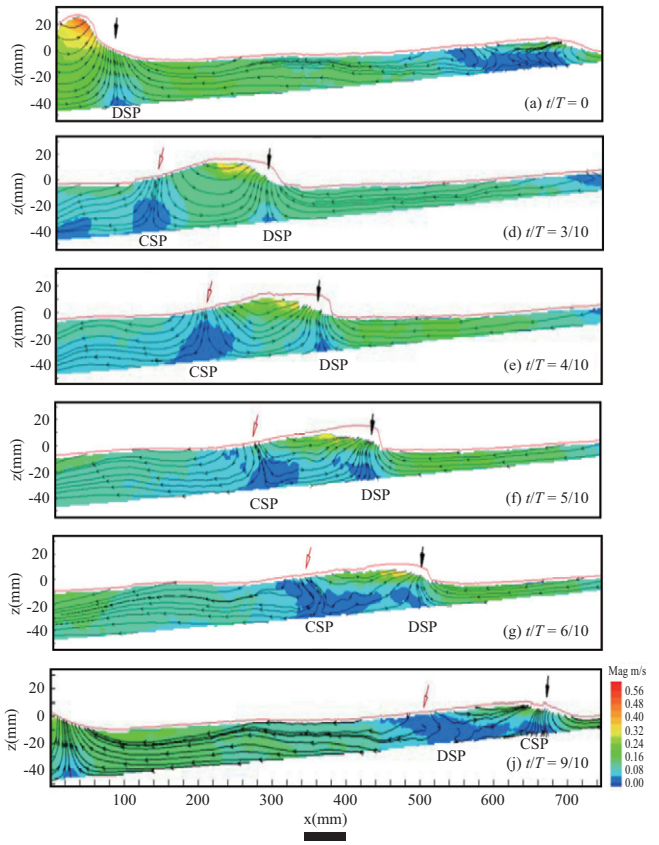

(c) Huang (2010)

Fig. 7. Comparison of computed streamline topography (black arrows) and velocity field (color contours) between (a) SP, (b) PL, and (c) Laboratory data of Huang (2010) (shown in Fig. 34 of Huang (2010)). Red and blue arrows indicate the locations of CSP and DSP near the sloping bottom, respectively. The colorbar has units of m/s.

mences and a DSP appears ahead of the wave crest, where the velocities are slower than that of the wave crest. The streamlines move vertically to a location near the wave crest, with streamlines belonging to the previous period's waves around x = 550~740 mm being relatively curved. At t/T = 3/10, the streamlines near the front of the wave crest become inclined because the wave crest touches the still water; at the same time, a CSP appears behind the bore front and the streamlines go nearly vertical down to the slope bottom. When the wave moves to t/T = 4/10 and t/T = 5/10, the upper streamlines moving to a CSP change their angle from vertical to around 130 degrees counterclockwise; the streamlines also become separated comparing to that of t/T = 3/10. At t/T = 6/10 and t/T = 9/10, the waves move to the inner surf zone, and the velocity field adjacent to the wave crest decreases gradually and becomes concentrated in the front of the wave crest. The next cycle of wave breaking is presented by a DSP generated around x = 40 mm (Fig. 7(a6)). Interestingly, there are two "eye-shaped" streamlines generated at this stage, oneclose to a CSP and the other close to a DSP. However, these streamlines are not seen in the data of Huang (2010).

The streamline topography of PL exhibits behavior similar to that of SP at the early stage of wave breaking. A DSP forms underneath the wave crest and the streamlines starting from the DSP move vertically toward the plunging tongue. Noticeably, at t/T = 3/25, there is an "aerofoil-type" streamline generated around x = 60~100 mm, where flow circulations are formed and velocities are lower than that of wave crest. It is also observed that the aerofoil-type streamlines pass over the DSP and move upstream at t/T = 4/25. A third PL appears at t/T = 11/25 due to the regeneration of the aerofoil-type streamlines. The generated aerofoil-type streamlines caused by the first wave breaking increasingly large and move along the slope bottom to a low-speed region near the location of the CSP (Figs. 7(b3) and (b4)). When waves move to t/T = 12/25, the interaction of low regions around x = 40~140 mm starts and the CSP moves onshore (Fig. 7(b5)). The streamlines near x = 40~140 mm become irregular, the streamline pattern is counterclockwise around x = 60~100 mm but clockwise around x = 100~140 mm. At t/T = 13/25, the CSP moves back to its initial position at t/T = 11/25 after interaction in low-speed regions.

Overall, a CSP (along the sloping bottom) always appears in the offshore direction after the generation of a DSP. The location of a DSP is generally underneath the front face of wave crest. Both DSP and CSP move to the inner surf zone following wave propagation. Furthermore, the velocities of reverse flows ahead of the wave crest are 0.15~0.2 m/s for SP and 0.25~0.3 m/s for PL, suggesting that PL contribute a stronger flow moving shore comparing to that of SP in the surf zone. Particularly, our results partially disagree with the laboratory results of Feng and Stansby (2005). Firstly, in the initial breaker, there is no DSP close to a plunging roller; instead, it appears near the slope bottom. Furthermore, a CSP always appears on the bed. Our results show flow circulation when waves propagate inland, which agrees with the findings of Feng and Stansby (2005) for a weak PL. The discrepancies may be partly caused by the flow structures of Feng and Stansby (2005) being based on a slowly varying wave assumption used for converting their temporal data to a spatial representation.

2. Vorticity Generation, Evolution and Corresponding Flow Structures

Fig. 8 shows a comparison of vorticity generation and evolution between SP and PL. Vorticity ω is defined as

$$\omega = \frac{\partial w}{\partial x} - \frac{\partial u}{\partial z} \tag{2}$$

where u and w are the mean fluid velocities in the x and z directions, respectively. Note that negative and positive values indicate vortices in the clockwise (CW) and counterclockwise (CCW) directions, entering in/pointing out of the paper, respectively. For SP, CW(-) vortices start within the front of the wave crest (t/T = 0/10) and gradually increase near

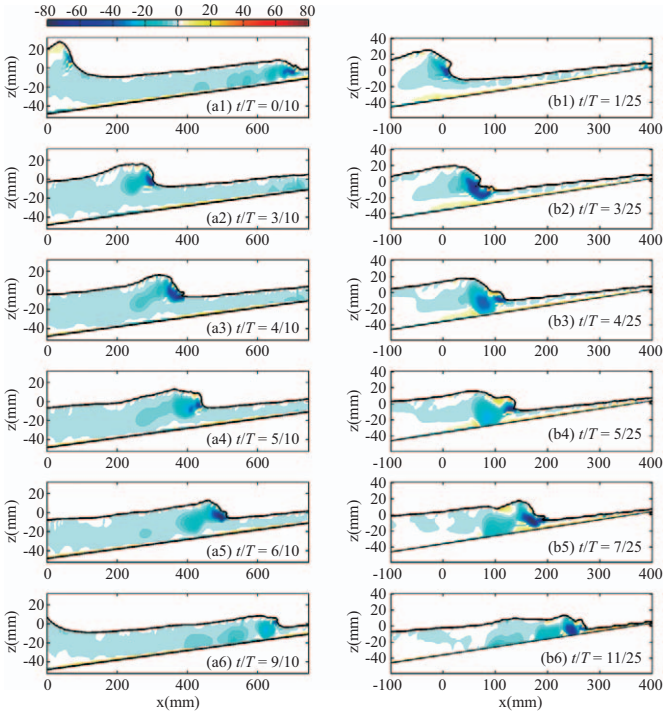

Fig. 8. Comparison of vorticity generation between (a) SP and (b) PL. The colorbar has units of s^{-1} Continued.

the front of the wave crest (t/T = 3/10 and t/T = 4/10). At the same time, there are scattered CCW(+) vortices near the free surface. Noticeably, certain CW(-) and CCW(+) vortices appear within thin layers near the bottom slope (t/T = 3/10 and t/T = 4/10). It indicates that a flow stagnation point and a DSP exists, causing flow separation due to the negative pressure gradient (Sou and Yeh, 2011). At t/T = 5/10 to t/T = 6/10, the CW(-) vortices start to separate and degenerate toward the offshore direction through advection and diffusion. The computed results indicate that the CW(-) vortices decay from the wave crest in the offshore direction by around 75%.

The initial stage of vorticity generation of PL is similar to that of SP (t/T = 1/25), where the CW(-) vortices start within the front of the wave plunger, but the magnitude is higher. Scattered CCW(+) vortices appear near the free surface. However, the generated CW(-) vortices are strong after the wave plunges into the front fluid (t/T = 3/25). At t/T = 3/25 to t/T = 5/25, certain CW(-) vortices with a strong magnitude aggregate where turbulent bores form. At the same time, the bulk CCW(+) vortices behind the top of the bore front with values on the order of O(20s^{-1}) are also observed. In addition, certain CW(-) and CCW(+) vortices in the onshore and offshore directions appear within thin layers near the bottom slope, respectively, which were also observed for SP. When bores move from t/T = 7/25 to t/T = 5/25 CCW(+) vortices increase again within the bore fronts because a secondary wave break commences, while the CCW(+) vortices close to the slope bottom and CW(+) vortices behind the bore front generated by the initial wave break start to decay upstream. At

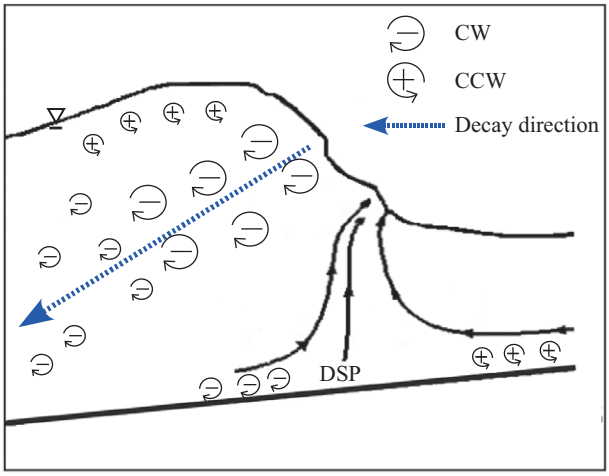

(a) SP

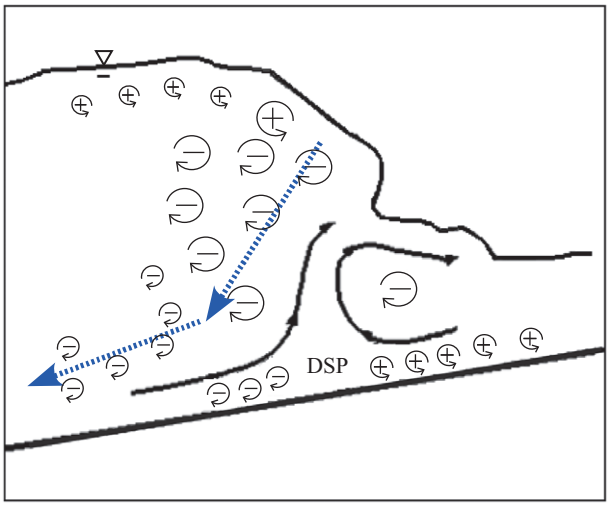

(b) PL

Fig. 9. Sketch of vorticity structure. (a) SP and (b) PL. The dashed arrow indicates the direction where CW(-) vortices decay.

t/T = 11/25, the CW(-) vortices due to secondary wave breaking degenerate toward the slope bottom and then decay in the offshore direction, repeating a cycle caused by the first breaking waves.

The vorticity structures and corresponding streamline topographies at the initial stage of SP and PL are quite different. Fig. 9 shows the difference in the outer surf zone, in which the free surfaces in Figs. 9(b) and (c) are drawn based on the numerical results of Fig. 7a(a3) and Fig. 7b(b2), respectively. Note that the circles representing CW(-) and CCW(+) vortices are of qualitative sketches to show the differences in magnitude. Generally, there are three similarities of vorticity for SP and PL: (1) CW(-) vortices of higher magnitude exist near the wave crest, (2) scattered CCW(+) vortices with a relatively weak magnitude appear near the free surface, and (3) certain CCW(+) and CW(-) vortices coexist in the onshore direction and offshore directions, respectively. However, there are strong CCW(-) vortices generated at the bore front after wave

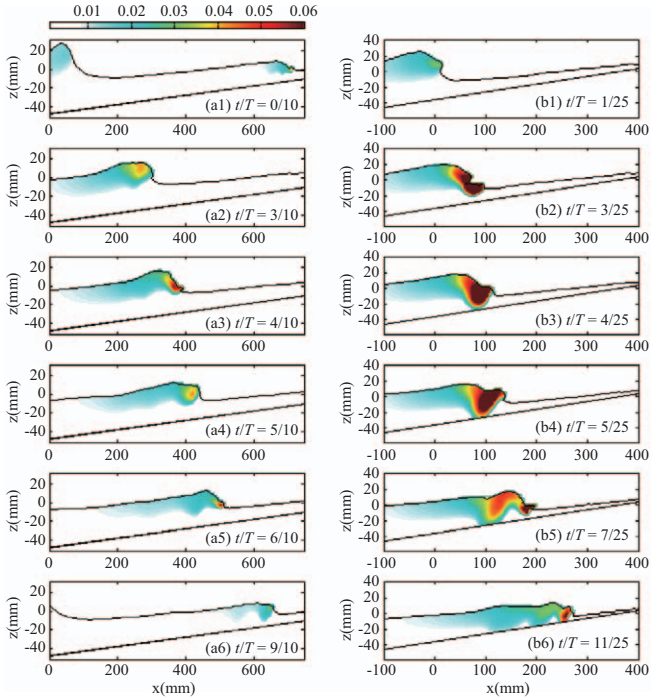

Fig. 10. Comparison of TKE evolution. (a) SP and (b) PL. The colorbar has units of m^2/s^2.

breaking for PL, whereas none are observed for SP. It is also noted that opposite vortices near the bottom induce the formation of a stagnation point where DSPs form. Nevertheless, the resulting streamlines of SP and PL near the bore front exhibit different shapes since the strong CCW(-) vortices at the bore front of PL change the fluid direction, causing significant reversal flows compared to that of SP (compare by Figs. 7(a3) and 7(b2)). Another difference between SP and PL is that the CW(-) vortices of SP decay gradually in the offshore direction but CW(-) vortices of PL advect toward the bottom slope and then degenerate upstream. Such flow properties imply that PL may contribute to a wave-driven scour near the bottom.

3. TKE

Fig. 10 shows a comparison of TKE values between SP and PL. The intensities of SP and PL are drawn using an identical colorbar for comparison. For SP, the TKE is generated near the wave crest, with a maximum intensity of around 0.015 m^2/sec^2 (~0.038 C^2), where $C = \sqrt{g(h+H)}$ is the propagation speed of a shallow water-wave. When the wave moves to t/T = 3/10 and t/T = 4/10, the TKE starts to overspread in the vicinity of the wave crest and to advect toward offshore. During this stage, the maximum TKE is around 0.058 m^2/sec^2 (~0.058 C^2), increasing almost quadruply compared to that at t/T = 0/10. At t/T = 5/10, the higher TKE convects toward the region of the white cap (see Fig. 3(c)) and then becomes concentrated in the front of the wave crest at t/T = 6/10. Note that at t/T = 6/10, the computed results suggest that the maximum

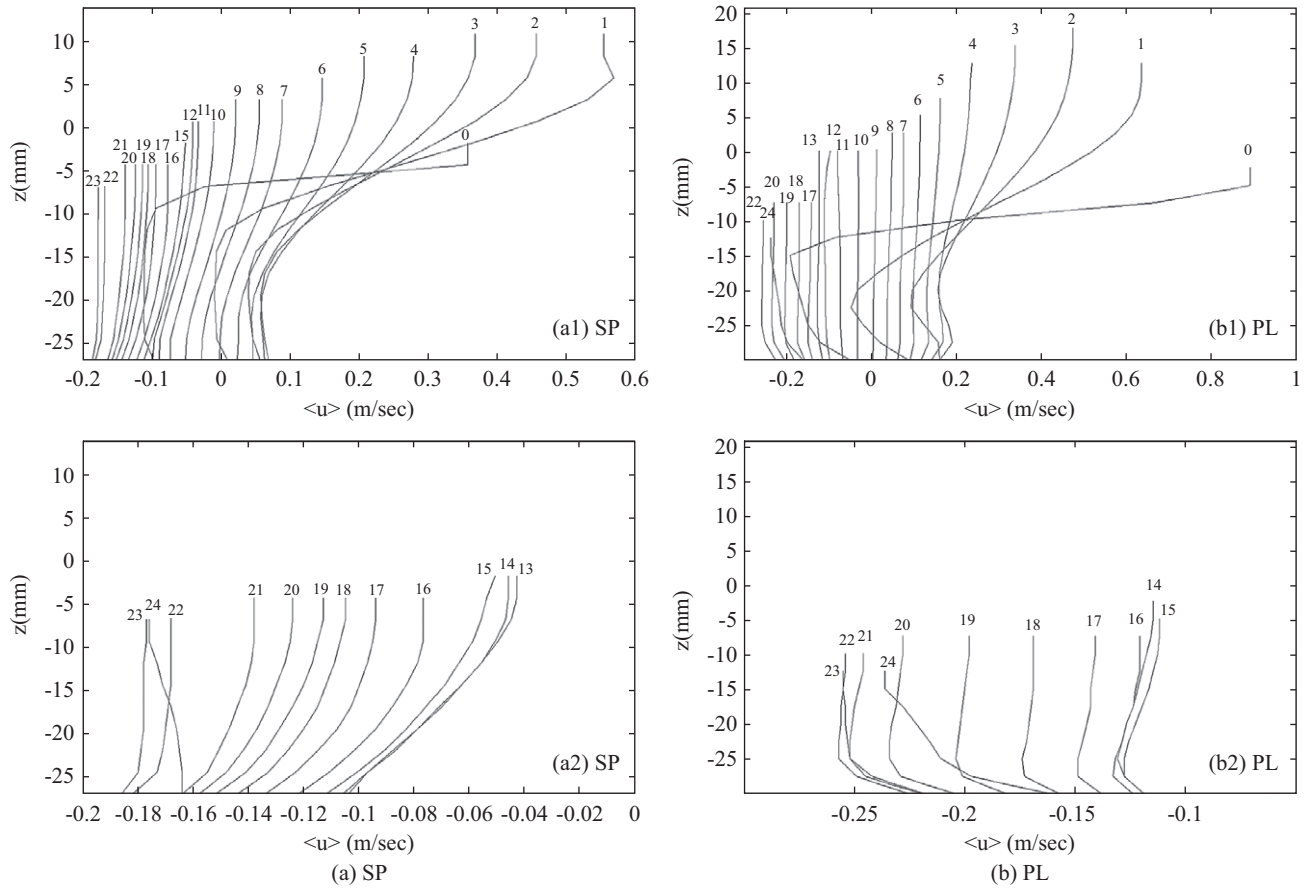

Fig. 11. Comparison of horizontal velocity profile between (a) SP (x = 390 mm; h = 2.85 cm) and (b) PL (x = 60 mm; h = 3.00 cm) waves. The numbers represent the phases (25t/T).

value of the front of the wave crest is around 0.048 m^2/sec^2 (~0.108 C^2), which is double that near the wave crest. At t/T = 9/10, the intensity decays to 0.032 m^2/sec^2 (~0.108 C^2).

The TKE intensity under PL-wave condition is relatively high (Fig. 10(b)). At t/T = 1/25, the wave breaking commences with an intensity of TKE of 0.032 m^2/sec^2 (~0.065 C^2). Noticeably, after the wave plunges into the front fluid, a maximum intensity of 0.21 m^2/sec^2 (~0.89 C^2) is observed at t/T = 3/25, which is over 4-fold higher than that of all maximum values under SP conditions. The TKE starts to advect toward the slope bottom at t/T = 4/25 and t/T = 5/25, exhibiting a similar behavior of vortex advection (Figs. 8(b3) and (b4)). Of note, at t/T = 7/25, the values of TKE between x = 135 to 190 mm approach zero and have a tendency towards upstream. A similar result was reported by Jiang et al. (2011). At t/T = 11/25, there exist two regions where the computed TKE values are almost zero due to secondary wave breaking.

Overall, for given wave conditions, the maximum TKE generated by PL is quadruple that generated by SP. The distributions of generated TKE values of SP and PL are similar to those of the corresponding vortices motions, which mirror a well-known phenomenon where turbulence generation always occurs following vortex generation. The TKE advects to the slope bottom for PL but is invisible for SP, which agrees with the results reported by Lubin et al. (2006).

4. Vertical Structure of Horizontal Velocity

The profiles of the horizontal velocity component over local water depths of SP and PL are shown in Fig. 11. Each number represents different phases of a 1/25 wave period (25 t/T = 1), where the numbers of zeros of SP and PL start at the locations shown in Fig. 7(a3) at t/T = 3/10 (x = 390 mm; h = 2.85 cm) and Fig. 7(b1) at t/T = 2/25 (x = 60 mm; h = 3.00 cm), respectively. Fig. 11(a) shows that on the incipient wave breaking, the horizontal velocities near the wave crest increase considerably from 0.35 to 0.56 m/s compared to that underneath the wave crest (t/T = 0/25, 1/25). In particular, at t/T = 7/25 the horizontal velocity near the bottom approaches zero, indicating that a stagnation point appears. Note that the horizontal velocities increase with decreasing water depth, explaining why the streamline topography curves have an angle (Fig. 7(a3)). Fig. 11a(a2) shows a close-up view of the reverse flow during the run-down phases. The horizontal velocities underneath the wave crest increase (toward the offshore direction) mainly due to the presence of reverse flow caused by wave run-down. However, the gravitational effects dominate

the increase (toward the offshore direction) of velocity in the following stages. The horizontal velocities eventually increase again due to the interaction of subsequent breaking waves (t/T = 23/25 to 24). Note that the horizontal velocities decrease with decreasing water depth and the magnitude of reverse flows could increase up to -0.18 m/s. Fig. 11(b) shows that the deformation of horizontal velocity of PL is relatively severe compared to that of SP (t/T = 0/25 to 3), which is caused by the strong reverse flows under a plunging wave (see Fig. 9(c)). It is also observed that the velocity gradient underneath the wave crest changes from $\partial u / \partial z < 0$ to $\partial u / \partial z > 0$ (t/T = 1/25, 2), which indicates that the CW(-) vortices near bottom change to CCW(+) vortices. A similar observation was reported by Sou and Yeh (2011). The stage at t/T = 9/25 suggests that a stagnation point exists; the velocity and associated gradient $\partial u / \partial z$ almost vanish. Interestingly, Fig. 11(b2) shows a different phenomenon of reverse flow compared to that of SP. The velocity increases (toward the offshore direction) with decreasing water depth (below z = −20 mm) but is relatively uniform underneath the wave trough (above z = −20 mm). The magnitude of reverse flows increases up to -0.25 m/s, which is around 1.4 times that of SP.

IV. CONCLUSION

The flow characteristics of spilling (SP) and plunging (PL) breakers in the surf zone were investigated using a Reynolds-averaged Navier-Stokes numerical model, COBRAS. The model simulation capability was validated by reproducing the spilling breaker experiment of Huang et al. (2009a). The good agreements between computed results and laboratory data indicate that the COBRAS model is capable of simulating flow characteristics in the surf zone under SP conditions. The effect of the beach slope on the flow characteristics in the surf zone of PL and SP under given wave conditions was investigated. The numerical results suggest the following main differences between SP and PL:

1. The streamline topography of PL is mostly similar to that of SP. For both types of breaker, a CSP always appears in the offshore direction after the generation of a DSP. The location of a DSP is generally underneath the front face of wave crest. Both DSP and CSP move to the inner surf zone following wave propagation.
2. The present numerical results of streamline topography partially disagree with those obtained by Feng and Stansby (2005). The discrepancies may be partly due to the flow structures of Feng and Stansby (2005) being based on a slowly varying wave assumption used for converting their temporal data to spatial representation.
3. The main difference of vortices is that CW(-) vortices after wave breaking are stronger for PL but mild for SP. The CW(-) vortices of SP decay upstream directly but those of PL advect toward the bottom slope and then degenerate upstream.
4. The TKE generated by PL is much larger than that generated by SP. The distributions of generated TKE values of SP and PL are similar to the corresponding vortex motions. The TKE generated by PL advects to the slope bottom for PL but is invisible for SP.
5. The main difference in reverse flow during run-down phases is that the horizontal velocities in the z-direction decrease with decreasing water depth for SP, whereas they increase for PL. The maximum magnitude of reverse flow of PL is around 1.4 times that of SP.

ACKNOWLEDGMENTS

This research was supported by National Science Council of Taiwan under grants NSC 101-2628-E-006-015-MY3, MOST 104-2911-I-006-301 (International Wave Dynamics Research Center), MOST 103-2221-E-006-229-MY3 and the Open Fund from the State Key Laboratory of Hydraulics and Mountain River Engineering, Sichuan University (SKHL1308).

REFERENCES

Battjes, J. A. (1974). Surf similarity. Proceeding of International Conference on Coastal Engineering. Copenhagen, Denmark, 466-480.

Battjes, J. A. (1988). Surf-zone dynamics. Annual Review of Fluid Mechanics 20, 257-293.

Bradford, S. F. (2000). Numerical simulation of surf zone dynamics. Journal of Waterway Port Coastal and Ocean Engineering-Asce 126, 1-13.

Chang, K. A. and L. F. Liu (1998). Velocity, acceleration and vorticity under a breaking wave. Physics of Fluids 10, 327-329.

Chang, K. A. and L. F. Liu (1999). Experimental investigation of turbulence generated by breaking waves in water of intermediate depth. Physics of Fluids 11, 3390-3400.

Christensen, E. D. (2006). Large eddy simulation of spilling and plunging breakers. Coastal Engineering 53, 463-485.

Christensen, E. D., D. J. Walstra and N. Emerat (2002). Vertical variation of the flow across the surf zone. Coastal Engineering 45, 169-198.

Dean, R. G. and R. A. Dalrymple (1991). Water-wave mechanics for engineers and scientists. World Scientific, River Edge, N.J.

Feng, T. and P. K. Stansby (2005). Streamline topography in periodic surf zone waves from LDA measurements. Measurement Science & Technology 16, 1929-1936.

Govender, K., G. P. Mocke and M. J. Alport (2004). Dissipation of isotropic turbulence and length-scale measurements through the wave roller in laboratory spilling waves. Journal of Geophysical Research-Oceans 109, 5115-5124.

Hsiao, S. C. and T. C. Lin (2010). Tsunami-like solitary waves impinging and overtopping an impermeable seawall: Experiment and RANS modeling. Coastal Engineering 57, 1-18.

Huang, Z. C., S. C. Hsiao and H. H. Hwung (2009a). Observation of Coherent Turbulent Structure Under Breaking Wave. International Journal of Offshore and Polar Engineering 19, 15-22.

Huang, Z. C., S. C. Hsiao, H. H. Hwung and K. A. Chang (2009b). Turbulence and energy dissipations of surf-zone spilling breakers. Coastal Engineering 56, 733-746.

Huang, Z. C. (2010). Experimental study of surf-zone dynamics and turbulence. Ph.D. Thesis, National Cheng Kung University, Tainan, Taiwan.

Jiang, C. B., J. Chen H. S. Tang and Y. Z. Cheng (2011). Hydrodynamic processes on beach: Wave breaking, up-rush, and backwash. Communications in Nonlinear Science and Numerical Simulation 16, 3126-3139.

Kimmoun, O. and H. Branger (2007). A particle image velocimetry investigation on laboratory surf-zone breaking waves over a sloping beach.

Journal of Fluid Mechanics 588, 353-397.
Lin, P. and L. F. Liu (1998a). A numerical study of breaking waves in the surf zone. Journal of Fluid Mechanics 359, 239-264.
Lin, P. and L. F. Liu (1998b). Turbulence transport, vorticity dynamics, and solute mixing under plunging breaking waves in surf zone. Journal of Geophysical Research 103, 15677-15694.
Liu, L. F. and I. J. Losada (2002). Wave propagation modeling in coastal engineering. Journal of Hydraulic Research. 40, 229-240.
Longo, S., M. Petti and I. J. Losada (2002). Turbulence in the swash and surf zones: a review. Coastal Engineering 45, 129-147.
Losada, I. J., J. L. Lara, R. Guanche and J. M. Gonzalez-Ondina (2008). Numerical analysis of wave overtopping of rubble mound breakwaters. Coastal Engineering 55, 47-62.
Lubin, P., S. Vincent, S. Abadie and J. P. Caltagirone (2006). Three-dimensional Large Eddy Simulation of air entrainment under plunging breaking waves. Coastal Engineering 53, 631-655.
Nadaoka, K., M. Hino and Y. Koyano (1989). Structure of the turbulent-flow field under breaking waves in the surf zone. Journal of Fluid Mechanics 204, 359-387.
Okayasu, A. (1989). Characteristics of turbulence structures and undertow in the surf zone. Ph.D Thesis, Yokohama National University, Yokohama, Japan.
Shin, S. and D. Cox (2006). Laboratory observations of inner surf and swash-zone hydrodynamics on a steep slope. Continental Shelf Research 26, 561-573.
Sou, I. M., E. A. Cowen and L. F. Liu (2010). Evolution of the turbulence structure in the surf and swash zones. Journal of Fluid Mechanics 644, 193-216.
Sou, I. M. and H. Yeh (2011). Laboratory study of the cross-shore flow structure in the surf and swash zones. Journal of Geophysical Research-Oceans 116, 15.
Stive, M. J. F. (1980). Velocity and pressure field in spilling breakers. Proceeding of International Conference on Coastal Engineering, Sydney, Australia, 547-566.
Ting, F. C. K. and J. T. Kirby (1994). Observation of undertow and turbulence in a laboratory surf zone. Coastal Engineering 24, 51-80.
Ting, F. C. K. and J. T. Kirby (1995). Dynamics of surf-zone turbulence in a strong plunging breaker. Coastal Engineering 24, 177-204.
Ting, F. C. K. and J. T. Kirby (1996). Dynamics of surf zone turbulence in a spilling breaker. Coastal Engineering 27, 131-160.
Wu, Y. T. and S. C. Hsiao (2013). Propagation of solitary waves over a submerged permeable breakwater. Coastal Engineering 81, 1-18.
Wu, Y. T., S. C. Hsiao, Z. C. Huang and K. S. Hwang (2012). Propagation of solitary waves over a bottom-mounted barrier. Coastal Engineering 62, 31-47.
Wu, Y. T., C. L. Yeh and S. C. Hsiao (2014). Three-dimensional numerical simulation on the interaction of solitary waves and porous breakwaters. Coastal Engineering 85, 12-29.
Zhang, Q. and L. F. Liu (2008). A numerical study of swash flows generated by bores. Coastal Engineering 55, 1113-1134.